

# Microscopic Description of Band Structure at Very Extended Shapes in the $A \sim 110$ Mass Region

Ching-Tsai Lee<sup>1</sup>, Yang Sun<sup>1</sup>, Jing-ye Zhang<sup>1</sup>, Mike Gudry<sup>1</sup>, Cheng-Li Wu<sup>2</sup>

<sup>1</sup>Department of Physics and Astronomy, University of Tennessee, Knoxville, Tennessee 37996

<sup>2</sup>National Center for Theoretical Science, Hsinchu, Taiwan 300, ROC

(February 9, 2020)

Recent experiment has confirmed the existence of rotational bands in the  $A \sim 110$  mass region with very extended shapes between super- and hyper-deformation. Using the projected shell model, we make a first attempt to describe quantitatively such a band structure in  $^{108}\text{Cd}$ . Excellent agreement is achieved in the dynamic moment of inertia  $\mathfrak{J}^{(2)}$  calculation, which allows us to suggest the spin values for the energy levels, which are experimentally unknown. It is found that at this large deformation, the sharply down-sloping orbitals in the proton  $i_{13/2}$  subshell are responsible for the irregularity in the experimental  $\mathfrak{J}^{(2)}$  and the wave functions of the observed states have a dominant component of two-quasiparticles from these orbitals. Measurement of transition quadrupole moments and g-factors will test these findings, and thus can provide a deeper understanding of the band structure at very extended shapes.

21.10.Re, 21.60.Cs, 23.20.Lv, 27.60.+j

Low-energy nuclear physics is characterized by a rich shell structure. A nuclear system can be stabilized at large deformations by quantum shell effects, leading to many observable phenomena. Nuclear super- and hyper-deformations have long been predicted to exist in nuclei. The study of superdeformed nuclei has been an active focus of low-energy nuclear physics for the past two decades. Today, superdeformation (SD) at high spin is not an isolated phenomenon, but instead is observed across the nuclear periodic table [1]. However, the field has been remained active because of the continuing discovery of new, exotic bands with distinct characteristic structures that one has never encountered before.

The very recent experimental work of Clark *et al.* [2] is such an example. Early calculations [3–5] suggested the likely regions where super- and hyper-deformation might exist. In particular, calculations predicted a very extended shape minimum in  $^{108}\text{Cd}$ , lying intermediate between super- and hyper-deformation, and the nuclei at this deformation are possibly stable against fission. In a recent letter [2], Clark *et al.* have found a rotational band in  $^{108}\text{Cd}$  with the data indicating that the nucleus has the most deformed structures identified to date.

An irregular pattern in dynamic moments of inertia ( $\mathfrak{J}^{(2)}$ ) was observed in this highly deformed band [2]. The experimental  $\mathfrak{J}^{(2)}$  curve begins with a large value ( $\approx 80[\hbar^2\text{MeV}^{-1}]$ ) at lower spins and quickly drops to 50. For the deduced transition quadrupole moment  $Q_t$ , the lower experimental limit was given as 9.5 eb [2]. Besides these global features, no detailed structure information is currently known for this band. This Rapid Communication aims to analyze the microscopic structure of this band and to explain the cause of the rapid change in  $\mathfrak{J}^{(2)}$ . Our calculations suggest that the low-K  $i_{13/2}$  proton orbitals are responsible for the  $\mathfrak{J}^{(2)}$  irregularity and that the two-quasiparticle configurations from these orbitals

dominate the structure of the observed states. Based on the excellent reproduction of the experimental  $\mathfrak{J}^{(2)}$ , we further suggest the spin values for the observed energy levels.

Our analysis is performed using the projected shell model (PSM) [6]. The PSM follows closely the shell model philosophy, and in fact, is a spherical shell model truncated in a deformed BCS single-particle basis. The truncation is first achieved within the quasi-particle basis with respect to the deformed BCS vacuum  $|0\rangle$ ; then rotational symmetry that is violated in the deformed mean-field basis is restored by standard angular-momentum projection techniques [7] to form a spherical basis in the laboratory frame; finally the shell model Hamiltonian is diagonalized in the projected basis. The truncation obtained in this way is very efficient, making a shell model calculation for a heavy, very deformed nucleus possible. Moreover, spin is a strictly conserved quantity in a theory with angular momentum projection. This is the most desired feature when applying a model to study SD structure because, for the most observed SD bands, it is very difficult, if not impossible, to determine spin values experimentally. In the past, the PSM was consistently applied for SD structure study to the mass regions  $A \sim 190$  [8,9],  $A \sim 130$  [10],  $A \sim 80$  [11],  $A \sim 60$  [12], and  $A \sim 30$  [13]. The predicted spin values for some SD bands were confirmed by later experiments.

In the PSM, the many-body wave function is a superposition of (angular momentum) projected multi-quasiparticle states,

$$|\psi_M^I\rangle = \sum_{\kappa} f_{\kappa} \hat{P}_{MK_{\kappa}}^I |\varphi_{\kappa}\rangle, \quad (1)$$

where  $\hat{P}_{MK}^I$  is the projection operator [7] and  $|\varphi_{\kappa}\rangle$  denotes basis states consisting of the quasiparticle (qp) vacuum, 2 quasi-neutron and -proton, and 4-qp states

$$|\varphi_\kappa\rangle = \{ |0\rangle, a_{\nu_1}^\dagger a_{\nu_2}^\dagger |0\rangle, a_{\pi_1}^\dagger a_{\pi_2}^\dagger |0\rangle, a_{\nu_1}^\dagger a_{\nu_2}^\dagger a_{\pi_1}^\dagger a_{\pi_2}^\dagger |0\rangle \}.$$

In Eq. (2),  $a^\dagger$ 's are the qp creation operators,  $\nu$ 's ( $\pi$ 's) denote the neutron (proton) Nilsson quantum numbers, which run over properly selected (low-lying) orbitals and  $|0\rangle$  is the qp vacuum (0-qp state). The dimensionality of the qp basis (2) is about 80 and the deformation of the basis is fixed at  $\epsilon_2 = 0.67$  for calculations in this paper. The choice of this deformation is based on experimental information [2]. We note that the choice of a basis deformation is not very sensitive for the PSM because the input deformation parameter serves to provide a good basis and the real deformation will be determined dynamically by a later configuration mixing.

For this  $N = 60$  and  $Z = 48$  nucleus with a large deformation, single-particle orbitals from several major shells can be found near the Fermi levels. Among them, the high- $j$  orbitals  $i_{13/2}$  and  $h_{11/2}$  are expected to play an important role for the structure of  $^{108}\text{Cd}$ . However, some orbitals from the major shells  $N = 4$  and  $N = 3$  also surround the Fermi levels. For a proper treatment, we have therefore included four major shells ( $N = 3, 4, 5$  and 6) each for neutrons and protons. This configuration space will ensure a correct description not only for the moment of inertia, but also for the quadrupole moment, which receives contributions from every individual nucleons. The importance of the neutron  $i_{13/2}$  and proton  $h_{11/2}$  orbitals was mentioned in Ref. [2]. However, we have found that the structure of the measured states is mainly determined by the  $i_{13/2}$  protons, as one will see below.

The same Hamiltonian (including spherical single-particle, residual quadrupole-quadrupole, monopole pairing, and quadrupole pairing terms) as employed in all of the early PSM work is then diagonalized in (1). The strength of the quadrupole-quadrupole force is determined in such a way that has a self-consistent relation with the quadrupole deformation  $\epsilon_2$  [6]. The monopole-pairing force constants  $G_M$  used in the present calculations are

$$G_M = [17.10 \mp 11.16 \frac{N-Z}{A}] A^{-1}, \quad (3)$$

with “-” for neutrons and “+” for protons, which are the same as those in the SD calculations for the  $A \sim 80$  mass region [11], and have an 8% reduction from the values used for the  $A \sim 190$  mass region [8,9]. Finally, the strength parameter  $G_Q$  for the quadrupole pairing is simply taken to be proportional to  $G_M$ . For the present calculation a standard proportionality constant of 0.16 is used.

With these at our disposal, we calculate energy levels of  $^{108}\text{Cd}$  for each spin and use the resulting wave functions to compute the matrix elements. In Fig. 1, the calculated energy levels are compared with data [2]. As in most SD band experiments, the spin value of the measured energy levels was not determined experimentally

(2) because lack of information of linking them to the known low-lying states. Assuming  $\mathfrak{J}^{(1)} \approx \mathfrak{J}^{(2)}$ , the authors in [2] estimated that the spin range for the 11 observed  $\gamma$ -rays is  $I = 40(2)\hbar - 60(2)\hbar$ . The calculated transition energies  $E\gamma$  are displayed in Fig. 1(a) together with data. The best fit between experiment and theory is achieved if we place the measured first  $E\gamma$  at  $I = 36\hbar$ . We regard this as fairly good agreement in spin values between our calculation and the experimental estimation.

Static and dynamic moments of inertia,  $\mathfrak{J}^{(1)}$  and  $\mathfrak{J}^{(2)}$ , are compared in Fig. 1(b). The characteristic feature is that the theoretical  $\mathfrak{J}^{(2)}$  exhibits a peak, starting from  $I = 10\hbar$  and ending at  $I = 50\hbar$ , with the centroid around  $I = 36\hbar$ . This corresponds to the clear slope change in the  $\mathfrak{J}^{(1)}$  curve in the same spin range. As can be seen, the measured  $\mathfrak{J}^{(2)}$  falls nicely onto the right side of the peak in the theoretical curve if the spin values  $I = 36\hbar$  for the measured first  $E\gamma$  is assumed. With the same assumption, the experimental  $\mathfrak{J}^{(1)}$  coincides with our calculated curve rather precisely.

The validity of the condition  $\mathfrak{J}^{(1)} \approx \mathfrak{J}^{(2)}$  can be further examined for the whole spin range. It is seen in Fig. 1(b) that the condition is nicely fulfilled at the beginning and at the end of the theoretical curves beyond the peak region. However,  $\mathfrak{J}^{(1)}$  and  $\mathfrak{J}^{(2)}$  differ strongly for a wide range of spin values in between. The measured cascade of  $\gamma$ -rays stops at the top of the peak and the experiment did not identify any further states along the left side of the  $\mathfrak{J}^{(2)}$  peak.

The existence of such a peak in  $\mathfrak{J}^{(2)}$  usually indicates a crossing of two (or more) bands with strong band interaction. The crossing can change the content of the wave functions for the spin states before and after the crossing. It is thus of interest to determine what the crossing bands are. To see this, a band diagram [6] is the most useful tool.

In the PSM, a band diagram is defined as the rotational energies of a set of bands calculated as the expectation values of the Hamiltonian with respect to projected quasiparticle states  $|\varphi_\kappa\rangle$  of Eq. (2). These are the basis bands before configuration mixing. Fig. 2 shows the band diagram from the current calculation. We plot the ground (0-qp) band, three important 2-qp bands, and two representative 4-qp bands. In addition, the lowest (yrast) states for each spin obtained from band mixing are plotted as dots. In this diagram, we look for bands that are the lowest in energy (thus most influential on the yrast states) in the spin range of interest. It can be seen that the three 2-qp states cross the ground band and become lower in energy at high spins. These are the two neutron 2-qp states of the  $i_{13/2}$  orbitals, coupled to  $(K = 1/2 \otimes K = 3/2)$  and  $(K = 3/2 \otimes K = 5/2)$  respectively, and one proton 2-qp states of the  $i_{13/2}$  orbitals, coupled to  $(K = 1/2 \otimes K = 3/2)$ . One sees that the proton 2-qp states (solid line in Fig. 2) define the lowest 2-qp band in the spin region where the first band crossing

occurs. The inset to Fig. 2 shows clearly that the proton 2-qp band crosses the ground band at  $I = 38\hbar$ . The other two 2-qp bands associated with  $i_{13/2}$  neutrons lie roughly 1 MeV higher than the proton 2-qp band and they cross the ground band at higher spin around  $I = 46\hbar$ . The 2-qp bands based on  $h_{11/2}$  protons (not shown in Fig. 2) lie even higher, about 2 MeV above the lowest proton  $i_{13/2}$  2-qp band. Thus, the band diagram tells us that the proton  $i_{13/2}$  2-qp states may be the dominant component in the observed band structure.

As one has seen in Fig. 1, the measured  $\gamma$ -rays are suggested to be in the spin range  $I = 36\hbar - 56\hbar$ . For this spin range, the proton 2-qp band is the lowest configuration, as shown in Fig. 2. We thus expect that the  $i_{13/2}$  protons with  $K = 1/2$  and  $3/2$  should strongly influence the high spin properties of the observed states, leading to additional observable phenomena. Electromagnetic transitions are important in understanding the underlying physics and in testing theoretical models. Transition quadrupole moments measure the contribution of many orbits to the collective structure. A large polarization effect is normally expected if the wave functions contain significant components from particular orbitals. This should be seen in calculations of the total electrical quadrupole moment. On the other hand, the g-factor is sensitive to the single-particle structure in wave functions. Because of the intrinsically opposite signs of the neutron and proton  $g_s$ , a study of g-factors enables determination of the microscopic structure. Therefore, we now discuss two additional physical quantities, the transitional quadrupole moment  $Q_t$  and the g-factor.

The transition quadrupole moment  $Q_t$  is related to the  $B(E2)$  transition probability through

$$Q_t(I) = \left( \frac{16\pi}{5} \frac{B(E2, I \rightarrow I-2)}{\langle IK20|I-2K \rangle} \right)^{1/2}. \quad (4)$$

The reduced transition probabilities  $B(E2)$  from the initial state  $\psi^{I_i}$  to the final state  $\psi^{I_f}$  are given by

$$B(E2, I_i \rightarrow I_f) = \frac{e_{\text{eff}}^2}{2I_i + 1} |\langle \psi^{I_f} | \hat{Q} | \psi^{I_i} \rangle|^2. \quad (5)$$

In the calculations, we have used effective charges ( $e_{\text{eff}}$ ) of 1.5e for protons and 0.5e for neutrons, which are the same as in the previous PSM calculations [6].

The g-factor can be expressed as

$$g(I) = \frac{\langle \psi_{M=I}^I | \hat{\mu}_z | \psi_{M=I}^I \rangle}{\mu_N I} = \frac{\langle \psi^I | \hat{\mu} | \psi^I \rangle}{\mu_N \sqrt{I(I+1)}}, \quad (6)$$

with  $\hat{\mu}$  the magnetic vector and  $\mu_N$  the nuclear magneton.  $g(I)$  can be written as a sum of proton and neutron contributions  $g_\pi(I) + g_\nu(I)$ , with

$$g_\tau(I) = \frac{1}{\mu_N \sqrt{I(I+1)}} \times \left( g_l^\tau \langle \psi^I | \hat{j}^\tau | \psi^I \rangle + (g_s^\tau - g_l^\tau) \langle \psi^I | \hat{s}^\tau | \psi^I \rangle \right), \quad (7)$$

where  $\tau = \pi$  or  $\nu$ , and  $g_l$  and  $g_s$  are the orbit and spin gyromagnetic ratios, respectively. We use the free values for  $g_l$  and the free values damped by the usual 0.75 factor for  $g_s$  [14]

$$\begin{aligned} g_l^\pi &= 1 & g_s^\pi &= 5.586 \times 0.75 \\ g_l^\nu &= 0 & g_s^\nu &= -3.826 \times 0.75. \end{aligned} \quad (8)$$

We emphasize [15] that the g-factor in the PSM is computed directly from the many-body wave function without a semiclassical separation of the collective and single-particle parts. In particular, because of the large configuration space employed, there is no need to introduce a core contribution,  $g_R$ , which is a model-dependent concept and not a measurable quantity.

The calculated  $Q_t(I)$  values are plotted in Fig. 3(a) as squares. Our calculation gives a constant value of 9.9 eb up to spin  $I = 20\hbar$ . A smooth increase follows until  $Q_t$  reaches the maximum value of 10.4 eb. These values are compared with the average value ( $> 9.5$  eb) from experiment [2]. The increase in  $Q_t$  (about 12% in the spin range roughly from  $I = 20\hbar$  to  $I = 50\hbar$ ) is associated with increased contribution of sharply down-sloping  $i_{13/2}$  orbitals. We note that a larger basis deformation  $\epsilon_2$  used for construction of the shell model space will in general give rise to a larger quadrupole moment calculated from the obtained wave functions. Here, what we believe is more important is the clear increase in  $Q_t$  near the band crossing region, a strong polarization by the sharply down-sloping particles. Usually, a band crossing will cause a drop in  $Q_t$  values.

To see that the major influence discussed above is mainly from the protons, not from the neutrons, we may study the rotational behavior of the g-factor. Due to the opposite sign of neutron and proton  $g_s$  in (8), effects originated from neutrons and protons should be easily distinguished. As shown by squares in Fig. 3(b), our calculations indicate a significant increase of the g-factor around the band crossing region. The increase is rather pronounced ( $\sim 25\%$ ). This indicates that starting from  $I = 20\hbar$ , components of the  $i_{13/2}$  protons become more and more dominant in the wave functions. In contrast, no increase can be seen if the proton 2-qp states are excluded from the calculation, as shown by the circles in Fig. 3(b). The slight decrease at higher spins is due to the fact that the neutron 2-qp states will first cross the ground band (at  $I = 46\hbar$ ) in the absence of the protons.

Thus, measurement of g-factors for several spin states and additional measurement of  $Q_t$  should be able to test our predictions and provide a deeper understanding of the measured band. Excited bands with very extended shapes in  $^{108}\text{Cd}$  might also be observed; our calculations show that these are likely to be mainly of neutron  $i_{13/2}$  2-qp structure (see Fig. 2).

In summary, using the projected shell model, which has been successfully applied to a microscopic descrip-

tion of nuclear superdeformed structure in several mass regions, we have studied the recently measured highly deformed rotational band in  $^{108}\text{Cd}$ . Our suggested spin values for the experimental levels are within 2 spin units of the experimental estimation. The observed irregularity in the dynamic moment of inertia is attributed to the quasiparticle alignment of  $i_{13/2}$  orbitals. Moreover, our calculations suggest that the important  $i_{13/2}$  configurations are not from neutrons, but from protons, and that the measured states have a proton  $i_{13/2}$  2-qp structure. Rotational behavior of  $Q_t$  and the g-factor has also been studied, with several predictions awaiting future experimental confirmation.

The present work has initiated a theoretical framework for a detailed structure study of nuclei with very extended shapes. One may expect that rotational bands in the neighboring nuclei could have similar properties and may be accessible by future experiment. Work on calculating neighboring nuclei is in progress. The present contribution has shown another example that the angular momentum projection is indeed a very efficient truncation scheme for a shell model calculation for medium or heavy nuclei with large quadrupole and pairing collectivities.

Research at the University of Tennessee is supported by the U. S. Department of Energy through Contract No. DE-FG05-96ER40983.

FIG. 1. (a) The calculated  $E_\gamma(I) = E(I) - E(I-2)$  (MeV) with the measured  $\gamma$ -ray energies [2] best fitted to the theory curve. (b) Comparison of the data [2] with the calculated static moment of inertia  $\mathfrak{S}^{(1)} = (2I-1)/E_\gamma(I)$  ( $\hbar^2\text{MeV}^{-1}$ ) and dynamic moment of inertia  $\mathfrak{S}^{(2)} = 4/[E_\gamma(I+2) - E_\gamma(I)]$  ( $\hbar^2\text{MeV}^{-1}$ ).

FIG. 2. A band diagram displaying rotational bands calculated for various multi-qp configurations. Dots are the Yrast band energies obtained after configuration mixing. Theoretical results presented in Fig. 1 are computed from these energies. The inset is an enhancement of the spin region around the first band crossing ( $I = 32\hbar - 42\hbar$ ).

FIG. 3. (a) The calculated transition quadrupole moments  $Q_t(\text{eb})$ . The experimental lower limit for the average  $Q_t$  is 9.5 eb [2]. (b) The calculated g-factors. For comparison, the rotor value  $Z/A$  is also shown.

- 
- [1] X.-L. Han and C.-L. Wu, At. Data Nucl. Data Tables **73**, 43 (1999); B. Singh, *et al.*, Nucl. Data Sheets, **78**, 1 (1996).
  - [2] R.M. Clark *et al.*, Phys. Rev. Lett. **87**, 202502 (2001).
  - [3] K. Neergard, V.V. Pashkevich and S. Frauendorf, Nucl. Phys. **A262**, 61 (1976).
  - [4] T. Werner and J. Dudek, At. Data Nucl. Data Tables **59**, 1 (1995).
  - [5] R.R. Chasman, Phys. Rev. **C64**, 024311 (2001).
  - [6] K. Hara and Y. Sun, Int. J. Mod. Phys. **E4**, 637 (1995).
  - [7] P. Ring and P. Schuck, *The Nuclear Many Body Problem* (Springer-Verlag, New York, 1980).
  - [8] Y. Sun, J.-y. Zhang and M. Guidry, Phys. Rev. Lett. **78**, 2321 (1997).
  - [9] Y. Sun, J.-y. Zhang and M. Guidry, Phys. Rev. **C63**, 047306 (2001).
  - [10] Y. Sun and M. Guidry, Phys. Rev. **C52**, R2844 (1995).
  - [11] C.-T. Lee, Master Thesis, National Sun Yat-sen University (2000), and to be published.
  - [12] Y. Sun, J.-y. Zhang, M. Guidry and C.-L. Wu, Phys. Rev. lett. **83** 686 (1999).
  - [13] G.-L. Long and Y. Sun, Phys. Rev. **C63** 021305(R) (2001).
  - [14] A. Bohr and B.R. Mottelson, *Nuclear Structure* (W.A. Benjamin, Inc., New York, 1975).
  - [15] Y. Sun and J.L. Egido, Nucl. Phys. **A580**, 1 (1994).

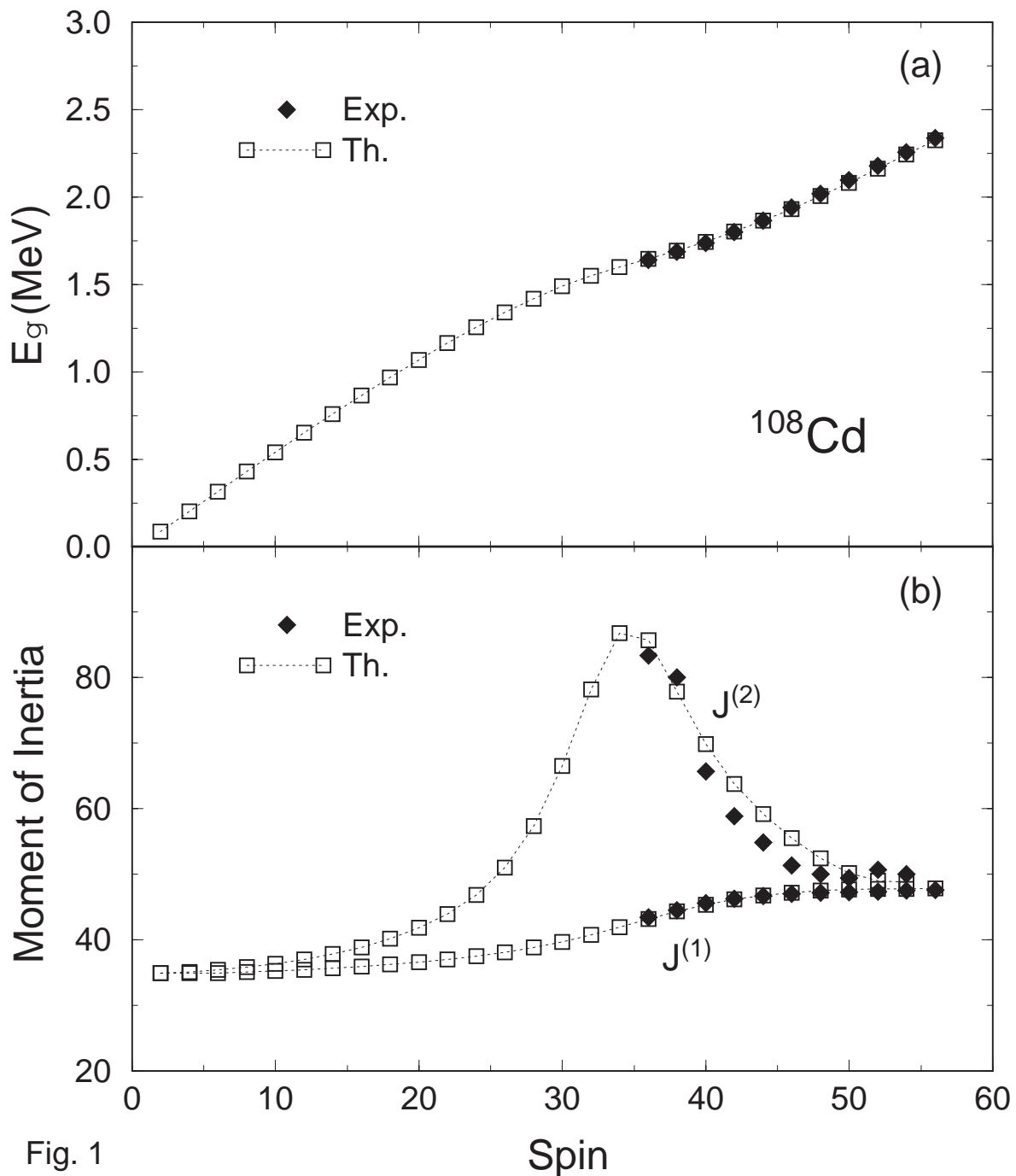


Fig. 1

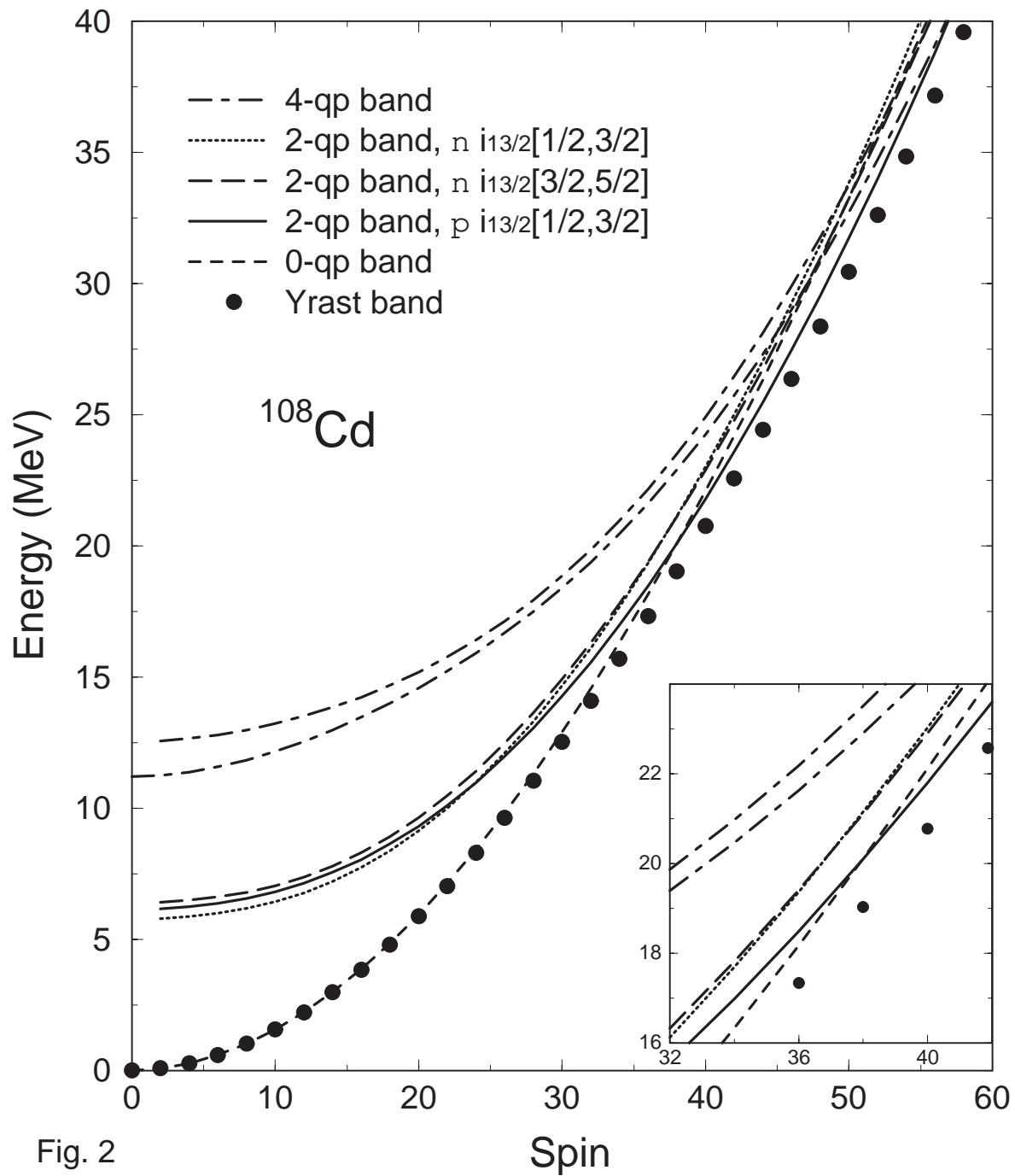


Fig. 2

